ADVANCED MATERIALS
www.advmat.de

A Cu-Based Near-IR Active MOF with an Ion-Pair Guest Exhibiting Versatile and Selective Gas-Solid Reactivity

Rajat Saha, Alejandro Cortés-Villena, Silvia Gómez-Coca, Alberto Fernández-Alarcón, Joaquín Calbo, Raquel E. Galian, Enrique Ortí, Eliseo Ruiz, Mónica Giménez-Marqués, Samia Benmansour,* and Carlos J. Gómez-García**

Metal–organic frameworks (MOFs) that react spontaneously and selectively with gases or vapors are useful in separation and purification processes, but are very scarce since only a few MOFs are capable of undergoing structural transformations. Simultaneous incorporation of cations and anions in a MOF is, as far as is known, never been observed. Here a new MOF: $(Me_2NH_2)(Cu^{I}Cl_2)@[Cu^{II}_4(INA)_4Cl_2O]\cdot 1.5dmf$ (3) (INA = isonicotinate, dmf = N,N'-dimethylformamide) is presented that simultaneously incorporates $Me_2NH_2^+$ cations and $CuCl_2^-$ anions. Furthermore, to the best of our knowledge, MOF 3 is the first transition metal-based near-IR active MOF. A systematic reactivity study with highly reactive gases and vapors shows that, in the presence of NH_3, MOF 3 presents a single-crystal-to single crystal transformation into $[Cu(INA)(OH)]\cdot H_2O$ (4-NH_3), a 3D MOF containing unprecedented $[Cu(\mu_3\text{-}OH)]_n^{n-}$ chains. With HCl or HCOOH vapors, MOF 3 shows a dissolution-recrystallization structural transformation into $(HINA)_2[Cu_2Cl_6(H_2O)_2]$ (5-HCl) or the 3D MOF $(Me_2NH_2)[Cu(HCOO)_3]$ (6-For). In contrast, MOF 3 remains stable under vapors of H_2SO_4, H_3PO_4, Et_3N, acetone, acetonitrile, methanol, ethanol, and pyridine. Theoretical calculations confirm the spontaneous nature of these transformations. Density functional theory (DFT) calculations show that the reduction of Cu^{II} to Cu^{I} in the host helps to explain such exceptional optical properties.

1. Introduction

Chemical reactivity is one of the fundamental properties of matter.[1,2] In gaseous and liquid phases, the reagents can move freely, allowing them to react spontaneously and homogeneously. In contrast, due to the compactness of the structures and strong interactions (covalent or ionic) between the components, solid-state materials are comparatively static in nature.[1,2] Although solid-phase reactions or transformations are well-known in organic chemistry,[3,4] they become very rare in inorganic materials, where their study is further limited by the absence of solid-state reactivity and the lack of stability of the single crystals in most cases.[5] Single crystals of inorganic materials may undergo such solid-phase chemical reactions in either restorative or disintegrative ways.[6,7]

Metal–organic frameworks (MOFs) and porous coordination polymers (CPs) are a special class of hybrid organic-inorganic materials, well-known for their regular and periodic structures. MOFs are constructed from metal ions or clusters and multi-topic organic linkers and have gained considerable attention for various applications based on their unique properties.[8–20]

Recently, MOFs and CPs have gained much attention for the utilization of their inherent regular, discrete cavities or channels to accommodate different types of guest molecules.[9,21–23] Within the confined space of the nano-sized cavities and channels of the host, the geometry, molecular orientation, supramolecular behavior, and

R. Saha, S. Benmansour, C. J. Gómez-García
Departamento de Química Inorgánica
Universidad de Valencia
C/ Dr. Moliner, 50, Burjasot (Valencia) 46100, Spain
E-mail: rajat.saha@uv.es; sam.ben@uv.es; carlos.gomez@uv.es

The ORCID identification number(s) for the author(s) of this article can be found under https://doi.org/10.1002/adma.202513485

DOI: 10.1002/adma.202513485

A. Cortés-Villena, A. Fernández-Alarcón, J. Calbo, R. E. Galian, E. Ortí, M. Giménez-Marqués
Institute of Molecular Science
University of Valencia
C/Catedrático José Beltrán Martínez 2, (Paterna) Valencia 46980, Spain

S. Gómez-Coca, E. Ruiz
Departament de Química Inorgànica i Orgànica and Institut de Recerca de Química Teòrica i Computacional
Universitat de Barcelona
Diagonal 645, Barcelona 08028, Spain

R. Saha
Department of Chemistry
Kazi Nazrul University
Asansol, West Bengal 713340, India

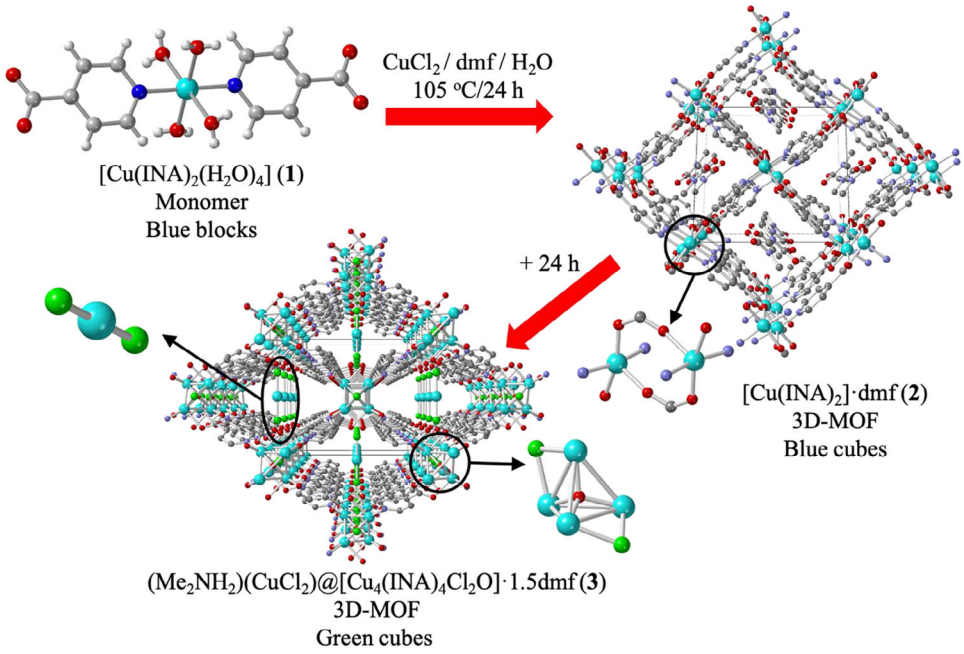

Figure 1. Synthesis of the 3D MOF **2** from monomer **1** and of the 3D MOF **3** from MOF **2**.

subsequent properties of the guest molecules may be different from those of the bulk phase.[24] Accordingly, guest@MOF may show some interesting functionalities different from those of the isolated guest and MOF, or even of the physical mixture of both.[25,26] The encapsulation of guests proceeds via molecular recognition at the pore surface and diffusion through the channels. Literature survey shows that several types of guest species, like metal cations, many different anions, metal nano-clusters, quantum dots, organic molecules, enzymes, drugs, inorganic complexes, polyoxometalates, organic polymers, etc., have been loaded within the channels or pores of different MOFs.[23] Albeit, as far as we know, no simultaneous encapsulation of cations and anions inside the cavity of a MOF has been reported. It should be noted that the presence of both cations and anions within the pores of MOFs may result in a host-to-guest or guest-to-host charge transfer that may lead to unusual functionalities such as electrical and/or proton conductivity, optical properties, redox activity, etc.[17,19,20,27] Here, we will show how, thanks to an in situ redox reaction, it is possible to generate, simultaneously, cations and anions inside a neutral MOF.

Solid-state reactivity of MOFs has become a major focus of research in recent years.[28–30] Several research groups have studied the solid-state structural transformation of MOFs under different external stimuli[31] like heat,[32,33] light,[34] pressure,[35] electrochemical,[36] chemical,[37] etc. In certain cases, drastic structural transformations have been observed, accompanied by changes in the coordination number,[38,39] geometry,[38–40] dimension,[39–41] topology,[42] interpenetration,[43] etc.[1,2,28–31] Vittal et al., and Bramer et al., have reviewed all types of possible structural transformations for MOFs and CPs.[1,28] Such structural transformations lead, in some cases, to unusual structures and functionalities that cannot be obtained by *de-novo* synthesis. In this regard, gas-solid reactions of MOFs leading to drastic structural transformations are very scarce due to the restricted movement of gas molecules within the void space of MOFs.[31]

In MOF reactivity, the most studied gas-solid reactions are those between MOFs and different solvent molecules in the gas phase, like water, methanol, or ethanol. For instance, upon exposure to moisture, $[Zn_4O(bdc)_3]$ (MOF-5, bdc = 1,4-benzenedicarboxylate) undergoes a structural transformation to $[Zn_3(OH)_2(bdc)_2]$ (MOF-69C) through cleavage of Zn-bdc coordination bonds and formation of metal-hydroxide bonds.[44] On the other hand, MIL-53 undergoes a pore size contraction due to the flexibility of the Cr-bdc bonds in the presence of moisture at room temperature.[45] There are other examples based on structural transformations without dimensionality change upon exposure to moisture. Thus, Brammer et al., reported the reversible structural transformation of the 1D CP $[Ag_4(O_2C(CF_2)_2CF_3)_4(TMP)_3]$ (TMP = 2,3,5,6-tetramethylpyrazine) into the 1D CP $[Ag_4(O_2C(CF_2)_2CF_3)_4(TMP)_3(EtOH)_2]$ in the presence of ethanol, and showed that, under HCl vapor, the metal-pyrazine bonds are cleaved when Cl^- coordinates to the metal centers and pyrazine groups get protonated.[46,47] These authors also performed mechanistic studies and theoretical calculations.[47] In a related study, Mínguez et al. demonstrated that the magnetic properties of a non-porous CP can be tuned by chemisorption of HCl,[48] and Adams et al. showed that the composition of the final product can be controlled by using different amounts of HCl and HBr.[49] Besides hydrogen halides, other gases, as NH_3 and $MeNH_2$, have also been reacted with different MOFs and CPs. Thus, Leznoff et al. studied the stepwise structural transformation of the 3D CP $Zn[Au(CN)_2]_2$ into the 1D CP $\{Zn(NH_3)_2[Au(CN)_2]_2\}$ and the monomer $Zn(NH_3)_4[Au(CN)_2]_2$ in the presence of NH_3 vapor,[50] whereas Li et al. reported the structural transformation of a non-porous 1D CP to a 3D porous supramolecular network upon exposure to methylamine vapor.[7]

Besides these single-crystal-to-single-crystal (SC-SC) transformations, dissolution-recrystallisation structural transformations (DRST) of MOFs have also become a major focus in MOF chemistry for developing new structures.[28,51] Most of the MOF-DRST reported to date are performed by solid-liquid reaction. For instance, Hupp and co-workers have studied the DRST-mediated conversion of EHU-30 to UiO-66 in the presence of acetic acid in N,N´-dimethylformamide (dmf) by in situ powder X-ray diffraction (PXRD) and in situ ^{1}H NMR spectroscopy.[52] Another interesting example of DRST was reported by Tu et al. These authors showed the interconversion of multiple zeolitic imidazolate frameworks (ZIFs) by the liquid-assisted DRST method.[53] Nevertheless, DRST of MOFs via gas-solid phase reactions is still very rare.[54]

Although, as discussed above, there are a few examples of gas-solid reactions leading to structural transformations in MOFs and even in molecular systems,[55–58] the number of reported examples is still very limited and, to our knowledge, no systematic study of the reactivity of a given MOF with different gases and vapor solvent molecules has been performed. To enlarge the knowledge about this unusual structural transformation of MOFs via gas-solid reactions, we have performed a systematic study of the gas-solid reaction of the Cu-containing MOF $(Me_2NH_2)(CuCl_2)@[Cu_4(INA)_4Cl_2O]\cdot 1.5dmf$ (**3**) with different gases and solvent vapors. This study shows that **3** undergoes versatile and selective structural transformation via both SC-SC and DRST in the presence of different gases and vapors. In particular, **3** reacts with 25% NH_3, HCl, HCOOH, and CH_3COOH vapors at room temperature within a few minutes (0.5–30 min, Figures S3–S6, Supporting Information). MOF **3** also reacts with HNO_3 vapors to yield a sea-green crystalline powder (Figure S7, Supporting Information), but remains stable in the presence of vapors of Et_3N, H_2SO_4, H_3PO_4, methanol, acetone, acetonitrile, and methanol for more than 7 days (Figures S8–S14, Supporting Information). Thus, the 3D MOF **3** shows, in the presence of 25% NH_3 vapor, a SC-SC transformation to the 3D MOF $[Cu(INA)(OH)]\cdot H_2O$ (**4-NH$_3$**), thanks to the selective reaction of MOF **3** with hydroxide ions, while it is stable for more than 7 days in Et_3N vapor. On the other side, MOF **3** transforms into the dimeric salt $(HINA)_2[Cu_2Cl_6(H_2O)_2]$ (**5-HCl**) upon exposure to aqueous HCl vapor within 5 min. In the presence of formic acid, HCOOH, MOF **3** converts into the 3D MOF $(Me_2NH_2)[Cu(HCOO)_3]$ (**6-For**) with selective capture of a dimethylammonium cation, $Me_2NH_2^+$, from the parent MOF. Finally, with acetic acid vapors, MOF **3** forms the well-known paddlewheel dimeric neutral complex $[Cu_2(CH_3COO)_4]\cdot 2H_2O$ (**7-Ac**).[59] We have performed theoretical calculations to identify the potential SC-SC and DRST mechanisms and the energy associated to all these structural transformations.

We have also studied the optical activity of MOF **3** in the UV–vis-IR range. Broad absorber materials from the UV to the mid-IR (MIR) and their emissive properties in the visible range have become a major focus in optoelectronics due to their potential applications, such as telecommunication, sensing, laser, biological imaging, and energy conversion, to name a few.[60,61] Generally, NIR-photoactive MOFs are synthesized by the utilization of NIR-active lanthanide ions[62–64] (Ln^{3+}, mostly Yb^{3+}, Nd^{3+}, and Er^{3+}) and organic chromophores as building blocks[65,66] or guest species.[67] The formation of extended charge transfer pathways within the MOF through encapsulation of redox-active guest species is another approach to develop NIR-active MOFs.[68,69] Besides, nanoparticles[70] or quantum dots[71] have also been used as the guest species to develop NIR-photoactive MOFs. As discussed below, the encapsulation of $CuCl_2^-$ within the void space of MOF **3** is responsible for the broad absorption from the UV to the MIR and up to 3000 nm and the emission in the visible range (480-550 nm). Density functional theory calculations show that the reduction of Cu^{II} to Cu^{I} in the host, under UV light irradiation, is the primary reason for such exceptional optical activity.

2. Results and Discussion

2.1. Synthesis of $(Me_2NH_2)(Cu^{I}Cl_2)@[Cu_4(INA)_4Cl_2O]\cdot 1.5dmf$ (3) from $[Cu(INA)_2]\cdot dmf$ (2) and $[Cu(INA)_2(H_2O)_4]$ (1)

Green cubic single crystals of the parent MOF $(Me_2NH_2)(Cu^{I}Cl_2)@[Cu_4(INA)_4Cl_2O]\cdot 1.5dmf$ (**3**) were synthesized by a two-step method. Initially, the solvothermal reaction at 105 °C of the monomer $[Cu(INA)_2(H_2O)_4]$ (**1**)[72–80] with $CuCl_2$ (1:1) in a 1:4 dmf-water mixture leads to the formation of blue cubic crystals of the 3D MOF $[Cu(INA)_2]\cdot dmf$ (**2**)[81,82] after 24 h (Figure S1, Supporting Information). Interestingly, extending the reaction for 24 h more, the blue cubic crystals convert into green ones of $(Me_2NH_2)(Cu^{I}Cl_2)@[Cu^{II}{}_4(INA)_4Cl_2O]\cdot 1.5dmf$ (**3**) (**Figure 1**), suggesting that compound **2** is the kinetic phase, whereas **3** is the thermodynamic one.

The transformation of **2** into **3** implies the aggregation of the carboxylate-bridged dimers into tetrahedral oxido-bridged tetramers, along with the inclusion of $CuCl_2^-$ anions and the reduction of the dmf molecules in **2** to $Me_2NH_2^+$ cations in **3**. Note that the formation of $Me_2NH_2^+$ cations from dmf under similar synthetic conditions is quite common,[83–85] and the reduction of Cu^{II} to Cu^{I} with dmf has also been previously observed.[82,86–90] We can, therefore, assume that the $Cu^{I}Cl_2^-$ anions located in the channels of **3** are formed by reduction of Cu^{II} with dmf when the solvothermal synthesis time is increased.

2.2. Versatile Structural Transformation of MOF 3 via both SC-SC and DRST into 4-NH3, 5-HCl, 6-For, and 7-Ac

When crystals of the parent MOF **3** are exposed to NH_3 in the gas phase, they transform into the 3D MOF $[Cu(INA)(OH)]\cdot H_2O$ (**4-NH$_3$**), which contains hydroxide-bridged Cu chains (**Figure 2**). In a similar way, exposing crystals of **3** to HCl, HCOOH, and CH_3COOH vapors, leads to crystals of the dimer $(HINA)_2[Cu_2Cl_6(H_2O)_2]$ (**5-HCl**), the 3D MOF $(Me_2NH_2)[Cu(HCOO)_3]$ (**6-For**), and the dimer $[Cu_2(CH_3COO)_4]\cdot 2H_2O$ (**7-Ac**), respectively (Figure S2, Supporting Information). These gas-solid state reactions occur within 30 min in all cases (Figures S3–S6, Supporting Information). Despite the reactivity of MOF **3**, it remains stable in the presence of vapors of Et_3N, H_2SO_4, H_3PO_4, methanol, acetone, acetonitrile, and methanol for more than 7 days (Figures S8–S14, Supporting Information). Note that compounds **3**, **4-NH$_3$**, **5-HCl**, and **6-For** are new, whereas **7-Ac** is the stable and well-known dimeric copper acetate compound.[59]

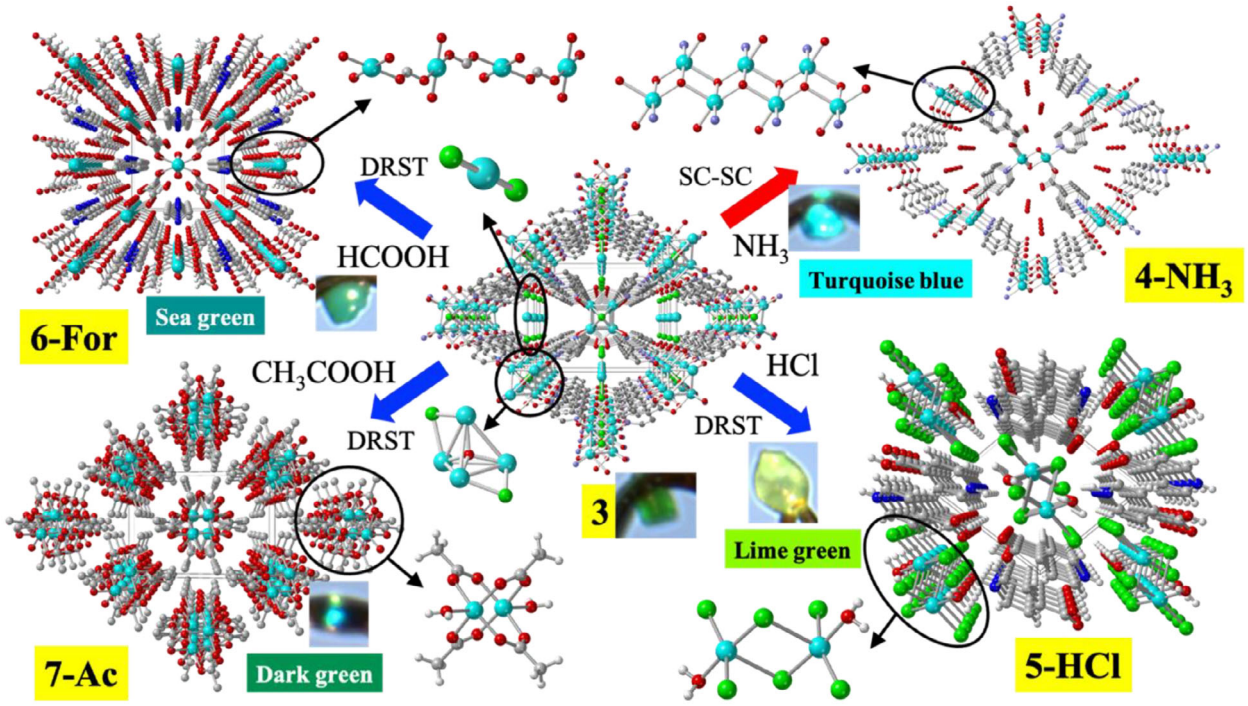

Figure 2. SC-SC and DRST of MOF **3** in the presence of vapors of NH_3, HCl, HCOOH, and CH_3COOH.

2.3. X-ray structure of $[Cu(INA)_2]$·dmf (2) and $(Me_2NH_2)(Cu^ICl_2)@[Cu_4(INA)_4Cl_2O]$·1.5dmf (3)

The crystal structure of the intermediate 3D MOF $[Cu(INA)_2]$·dmf (**2**) has already been reported[81] and, therefore, here we will only describe it briefly to decipher the mechanism of the transformation **2** → **3**. MOF **2** consists of a 3D lattice formed by double carboxylate-bridged Cu^{II} dimers that are further connected by isonicotinate bridges (Figure S15, Supporting Information), giving rise to square channels running along the *a*-axis containing the dmf solvent molecules (Figure S16, Supporting Information). The carboxylate-bridged Cu dimers are located at the vertices of the squares, with the INA^- bridges forming the sides and connecting each dimer to four other dimers in the four closest corners (Figure S16, Supporting Information). The Cu^{II} ions are surrounded by five different INA^- ligands and show a CuN_2O_3 square pyramidal coordination geometry. The basal plane contains two *trans* N-atoms and two *trans* O-atoms, whereas the axial position is occupied by an O-atom (Figure 1).

Single-crystal X-ray diffraction (SCXRD) analysis shows that MOF **3** crystallizes in the chiral orthorhombic space group *I*222 and presents a 3D structure (Table S1, Supporting Information). The asymmetric unit contains one INA^- ligand and one Cu^{II} metal center (Cu1), both on general positions, one O atom (O2), and one chloride ligand (Cl1), both located on a two-fold axis and coordinated to Cu1. There is also a Cu^I atom (Cu10) located on a two-fold axis and one chloride ligand (Cl10) coordinated to Cu10 (Figure S17, Supporting Information). It also contains one $Me_2NH_2^+$ cation and one and a half dmf molecules delocalized in the voids, as indicated by the thermogravimetric and elemental analysis (see Supporting Information), and by the Mask and Squeeze procedures (see below), resulting in the formula $(Me_2NH_2)(Cu^ICl_2)@[Cu^{II}{}_4(INA)_4Cl_2O]$·1.5dmf (**3**). The central tetrahedral $[Cu_4OCl_2]$ unit is formed by a central μ_4-O atom (O2) coordinated to the four Cu centers and by two bridging chlorides at the outer periphery (**Figure 3**). Each copper shows a five-coordinated square pyramidal geometry formed by the coordinated central oxygen atom (O2), one chloride atom (Cl1), two carboxylate oxygen atoms (O1 and O11) of two different INA^- ligands and one pyridyl N-atom (N1) of a third INA^- ligand (N1), with the axial position occupied by O11 (Figure 3). Each INA^- ligand binds to three different metal centers: two Cu1 from a Cu_4O cluster with the two carboxylate O-atoms (O1 and O11) and one Cu1 atom from a neighboring Cu_4O cluster with the N atom (N1, Figure S18, Supporting Information). In this way, each Cu_4O cluster is connected to eight neighboring similar clusters through eight different INA^- bridges to form an overall *bcu*-3D framework (Figure S19, Supporting Information). The bond distances and angles around the Cu1 atom (Tables S2 and S3, Supporting Information) are the typical ones for penta-coordinated Cu^{II} centers with square pyramidal geometry and, as expected, the axial Cu-O11 bond distance (2.304(3) Å) is longer than the equatorial ones (in the range 1.909–1.969 Å). The Cu10-Cl10 bond distance (2.101(3) Å) is in the normal range observed for other similar linear $CuCl_2^-$ anions.[90–97] The oxidation state of the Cu ions in this (and all the other compounds) has been confirmed by bond valence sum calculations (Table S10, Supporting Information).

It is noteworthy that a very similar structure has been reported by Bai et al., although without the $Me_2NH_2^+$ cations and the solvent molecules inserted in the cavities of the MOF.[82] In our case, the framework contains a large void space of 931 $Å^3$ per unit cell (44% of the unit cell volume), where it accommodates a

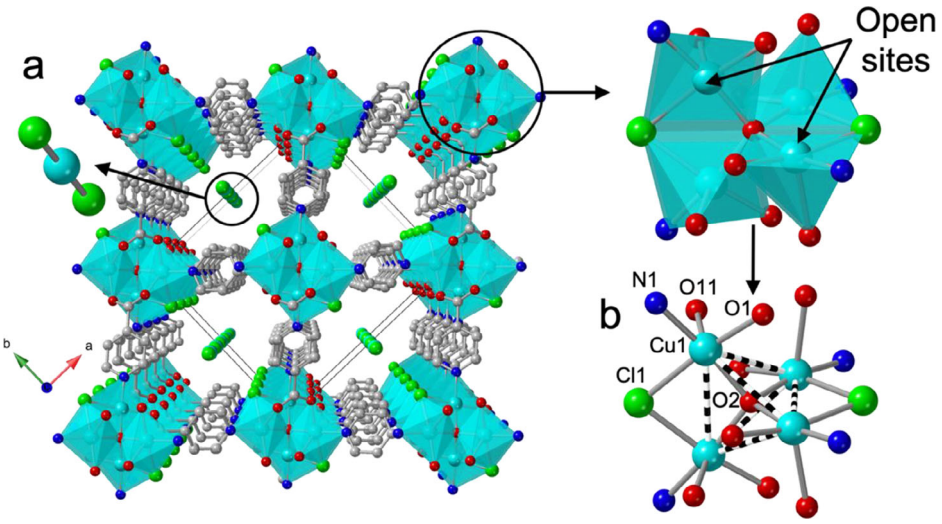

Figure 3. a) Perspective view of the structure of MOF **3** down the *c* direction. b) Detail of the Cu_4OCl_2 central cluster with the labelling scheme.

linear $CuCl_2^-$ anion with the Cu^I ion sitting on a two-fold axis, a disordered $Me_2NH_2^+$ cation, and one and a half disordered solvent dmf molecules. Since the framework $[Cu_4OCl_2(INA)_4]$ is neutral, the insertion of the $CuCl_2^-$ anion requires a charge-compensating cation. Note that the formation of $Me_2NH_2^+$ from dmf under the same conditions has been observed in many cases[83–85] and, therefore, we can assume that $Me_2NH_2^+$ must be the charge-compensating cation in our case. Application of Squeeze and Mask procedures to the X-ray data shows the presence of a total of 88 e^- per formula unit, which corresponds to one $Me_2NH_2^+$ cation and 1.5dmf molecules per formula unit (accounting for 86 e^-). These data agree with the thermogravimetric analysis (Figure S20, Supporting Information), which shows a progressive mass release of ≈18% in the temperature range 50–250 °C, corresponding to the loss of one Me_2NH, one HCl, and one and a half dmf molecules (calculated = 17.2%). Above ≈270 °C, the sample decomposes as a result of the decomposition of the INA^- ligands.

The most original feature of this 3D framework is the fact that the neutral framework contains simultaneously both, an inserted cation and an anion within the void space, providing a charge transfer pathway through the channel. The presence of unsaturated metal centers and labile bridging chlorides prompted us to attempt some post-synthetic modification using both solution and vapor phase (see below).

Bulk purity of the framework was analyzed by powder X-ray diffraction (PXRD) (Figure S21, Supporting Information). In order to assess the presence of Cu^{II} in MOF **3**, we carried out EPR and magnetic measurements as well as bond valence sum calculations (Table S10, Supporting Information).

2.4. Characterization of $[Cu(INA)_2]$·dmf (2) and $(Me_2NH_2)(Cu^ICl_2)@[Cu_4(INA)_4Cl_2O]$·1.5dmf (3)

The EPR study of **2** and **3** (Figure S22, Supporting Information) is very similar and shows the expected axial signals for square pyramidal Cu^{II} ions. In **3** we do not observe any extra signal from the $CuCl_2^-$ units, in agreement with the Cu^I oxidation state of the copper center in this linear anion. The presence of neutral $CuCl_2$ can also be discarded from the EPR spectrum.

The magnetic properties of compound **2** (Figure S23, Supporting Information) show that it behaves as an antiferromagnetic Cu^{2+} dimer with a weak antiferromagnetic coupling (see Table S11, Supporting Information), in agreement with the expected behavior for a double *syn-syn* carboxylate bridge connecting axial and basal positions. The magnetic properties of **3** further confirm that the Cu_4O central cluster contains Cu^{2+} ions, whereas the inserted $CuCl_2^-$ anions contain diamagnetic Cu^I. The central Cu_4O cluster presents three different Cu···Cu interactions, two are antiferromagnetic and one ferromagnetic (Figure S24 and Table S11, Supporting Information), leading to a diamagnetic ground state with two spins up and two down (see inset in Figure S24, Supporting Information).

X-ray photoelectron spectroscopy (XPS) analysis shows the presence of two close peaks at 952.2 and 954.0 eV for Cu $2p_{1/2}$ and, similarly, two peaks at 932.4 and 934.8 eV for Cu $2p_{3/2}$ (Figure S25, Supporting Information). This indicates the presence of two different copper species within compound **3**. The higher energy peaks correspond to Cu^I, and the lower energy peaks result from the Cu^{II} species.

Field emission scanning electronic microscopy (FESEM) images (Figure S26, Supporting Information) and the energy-dispersive X-ray spectroscopy analysis (EDAX, Figure S27, Supporting Information) confirm the presence of the corresponding elements in the elemental mapping and their homogenous distribution (Figure S28, Supporting Information).

The porosity of the activated MOF **3** was first examined by volumetric N_2 gas sorption experiments at 77 K, resulting in negligible adsorption, as expected for narrow-pore materials. To access the narrow porosity, gravimetric CO_2 gas sorption experiments were conducted at 273 K and relatively high pressures. Moderate CO_2 uptake of ≈0.6 mmol CO_2 g^{-1} was obtained at $p(CO_2) = 10$ bar (Figure S29, Supporting Information).

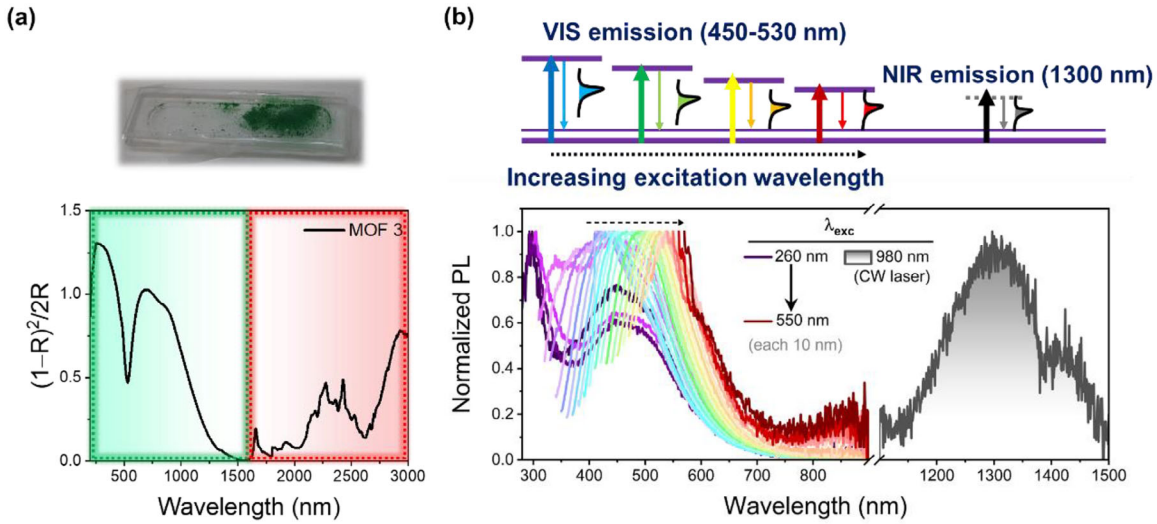

Figure 4. a) Picture of MOF **3** powder (top) and diffuse reflectance spectrum covering from the UV to the NIR-MIR spectral region (bottom). b) Schematic representation of the observed trend between emission wavelength as a function of the excitation wavelength (top) and normalized photoluminescence (PL) spectra under different excitation wavelengths (bottom) in the VIS and NIR spectral range.

2.5. Steady-State and Time-Resolved Spectroscopy Studies of MOF 3

To the best of our knowledge, there is no report on the usage of small inorganic molecules as guests within the void space to tune the MOF's optical properties to date. Several reports have already explored the unusual optical and electrical properties of copper(I) halides.[98,99] So, it might be interesting to study the optical activity of MOF **3** due to the nanoconfinement of $CuCl_2^-$. The presence of both $CuCl_2^-$ and $Me_2NH_2^+$ within the MOF may cause charge transfer interactions within the framework.

The diffuse reflectance spectrum of MOF **3** (**Figure 4a**) obtained through the Kubelka-Munk function [KM = $(1\text{-}R)^2/2R$] in solid state at room temperature shows different features: strong and broad optical transitions in the UV–Vis, and moderate transitions in the near-Infrared (NIR, 750–2500 nm)-mid-Infrared (MIR, > 2500 nm) spectral range. These optical transitions in the visible spectral range are clearly evidenced by the distinctive green color of the powder (see Figure 4a, top). The absorption maximum in the UV window is located at ≈270 nm and is assigned to π–π^* transitions in the linker as previously observed,[100] whereas the broad and featureless absorption in the visible region peaking at 690 nm may originate from a mixture of ligand-to-metal charge transfer (LMCT), metal-to-ligand charge transfer (MLCT), and metal cluster-centered transitions (MCCT) within the MOF.[100–104] Moreover, the transitions in the NIR-MIR region (1600 up to 2900 nm) could be assigned to optical transitions of inter-valence charge-transfer (IVCT) from Cu^I ($3d^{10}$) to Cu^{II} ($3d^9$).[105]

The steady-state photoluminescence (PL) properties were recorded upon excitation of MOF **3** at room temperature with different excitation wavelengths, from 260 to 550 nm, as shown in Figure 4b. Under excitation at high energies (260-280 nm), the PL spectrum exhibits two clear emission bands, at ≈300 and 450 nm, the higher-energy one being more intense, indicating the presence of two emitting states. These two emissions could originate from different mechanisms, as their photoluminescence excitation (PLE) spectra differ substantially (see Figure S30, Supporting Information). The higher-energy band emerges from π–π^* transitions in the linker.[106] Above 300 nm excitation, the lower-energy band becomes more intense, redshifted, and dependent on the excitation wavelength, suggesting that the resulting emission presumably arises from a mix of charge-transfer states, i.e., LMCT and MCCT, which explains the large bathochromic shift.[105] Therefore, Cu···Cu distances seem to play a key role in the photophysical properties of the MOF.[107] It is noteworthy that no emission in the visible range was registered above 530 nm excitation. This excitation-dependent emission behavior has been rarely reported in MOF materials and could be associated with the complex nature of the emitting states in MOFs,[108] and the presence of multiple low-lying singlet emissive states (see Figure 4b, top, Figure S31, Supporting Information). Moreover, the significant bathochromic shift was confirmed by recording the PLE spectra of MOF **3** at different emission wavelengths, from 290 to 580 nm. Indeed, at high emission wavelengths, the maximum showed a broadening and a bathochromic shift up to 375 nm (Figure S30, Supporting Information). Interestingly, under 980 nm continuous-wave (CW) laser excitation (2 W), MOF **3** produces a weak, but notable emission in the NIR centered at 1300 nm (Figure 4b), indicating the presence of LMCT states that enable low-energy emission pathways in the NIR within the Cu-based framework (note that no NIR emission was detected under continuous xenon lamp excitation).

The time-resolved PL properties of MOF **3** were also recorded at three emission maxima (480, 520, and 550 nm) by using pulsed-laser excitation wavelengths of 400, 450, and 500 nm, respectively, to study the dynamics of the emissive states. The emission spectra under these excitation conditions are displayed in Figure S32a (Supporting Information), where the bathochromic

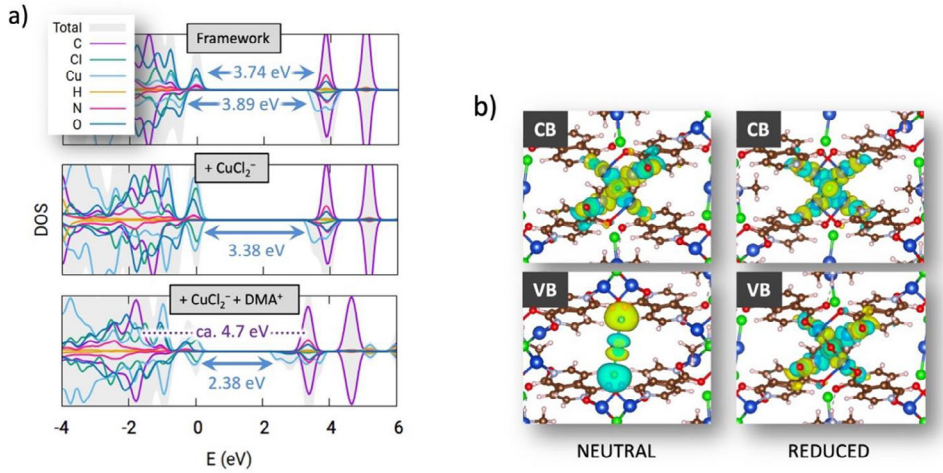

Figure 5. a) Species-projected density of states of the framework of MOF **3**, and after including $CuCl_2^-$ and $Me_2NH_2^+$ guest ions, calculated at the hybrid-DFT HSE06 level of theory. b) Frontier crystal orbitals (spin-β channel) calculated for **3** in its neutral form and upon one-electron reduction.

shift of the emission is clearly appreciated. Fitting to a biexponential decay function to all decay traces (Figure S32b, Supporting Information), two emission lifetimes of 2.32 ± 0.01 (58%) and 7.24 ± 0.05 ns (42%) were obtained, indicating the presence of two main allowed transitions involved within this broad band of fluorescence in nature.

2.6. Electronic Structure Calculations on MOF 3

To shed light on the optical activity of MOF **3**, a thorough theoretical DFT characterization was performed using the all-electron, full-potential FHI-aims electronic structure code (see the Supporting Information for full computational details).[109] MOF **3** is a 3D framework based on Cu^{II} secondary building units (SBU), INA^- ligands, and $CuCl_2^-$ and $Me_2NH_2^+$ as guest ions. The species-projected density of states of the framework of MOF **3**, calculated at the hybrid-DFT HSE06 level of theory,[110] shows that the pristine framework presents a large direct bandgap of 3.74(α)/3.89(β) eV described by a valence band (VB) centered at the Cu^{II}-based SBU and a conduction band (CB) centered at $INA^-(\alpha)/Cu^{II}(\beta)$ (**Figure 5**a; Figures S33 and S34, Supporting Information). Introduction of $CuCl_2^-$ inserts energy levels slightly above the VB (Figure 5a; Figures S35 and S36, Supporting Information) and reduces the bandgap to 3.38 eV (spin-β channel). Additionally, the presence of $Me_2NH_2^+$ promotes a strong reduction of the bandgap, predicted at 2.38 eV for the full system **3** (Figure S37, Supporting Information). The $Me_2NH_2^+$ energy levels are located far away from the bandgap edges, so we ascribe such electronic effect to a change in the crystal structure of the framework, which splits both the $CuCl_2^-$ occupied levels in the VB and the Cu^{II}-centered empty levels in the CB (Figure 5a). Analyzing the minimum-energy geometry of **3**, we find that insertion of $CuCl_2^-$ causes a slight contraction of the unit cell, suggesting that it interacts attractively with the framework through electrostatic forces (Table S12, Supporting Information). On the other hand, the addition of $Me_2NH_2^+$ leads to a large anisotropic structural change with lateral expansion (lattice directions *a* and *b*) and vertical compression (direction *c*), pointing to a reorganization of the host framework to accommodate the organic cation. The theoretical lattice parameters predicted for **3** (including $CuCl_2^-$ and $Me_2NH_2^+$) are in very good agreement with the experimental data (Table S12, Supporting Information).

Comparison between the experimental data and the theoretical energy levels allows us to assign the nature of the electronic transitions that give rise to the optical features observed in the absorption spectrum of **3**. First, we predict an energy difference of ≈4.7 eV between the occupied and unoccupied crystal orbitals with major participation of the organic ligand INA^- (peaks with large carbon contribution; Figure 5a), which nicely correlates with the intense absorption band experimentally centered at 270 nm (4.6 eV). On the other hand, the absorption band recorded at around ≈690 nm is assigned to the VB → CB transition (2.38 eV), which is associated with electronic promotions from the $CuCl_2^-$ guest to the unoccupied Cu^{II}-*d* levels of the framework, therefore showing a strong charge-transfer character (Figure 5b).

The presence of absorption bands experimentally recorded above 1000 nm may correspond to states promoted by the Cu^I/Cu^{II} accessible redox pair. In fact, we predict that the CB of MOF **3** centered at Cu^{II} is located as deep as −4.83 eV, indicating that reduction of Cu^{II} to Cu^I is likely to occur. Hence, we modelled MOF **3** upon one-electron reduction, and Mulliken analysis of the accumulated charges evidences that the extra electron is collected mostly on the framework (−0.93 e). A large electron affinity of 4.41 eV is predicted for the one-electron reduction process, which confirms the thermodynamic driving force for electron uptake. In this reduced system, the bandgap nature is fully described by the framework of **3**, with both the VB and CB centered on the Cu-based SBU (Figure 5b, Figures S38 and S39, Supporting Information). We predict a small energy of 0.61 eV for this mixed-valence $Cu^I \rightarrow Cu^{II}$ transition, thus supporting the NIR-MIR optical activity recorded experimentally (Figure S40, Supporting Information).

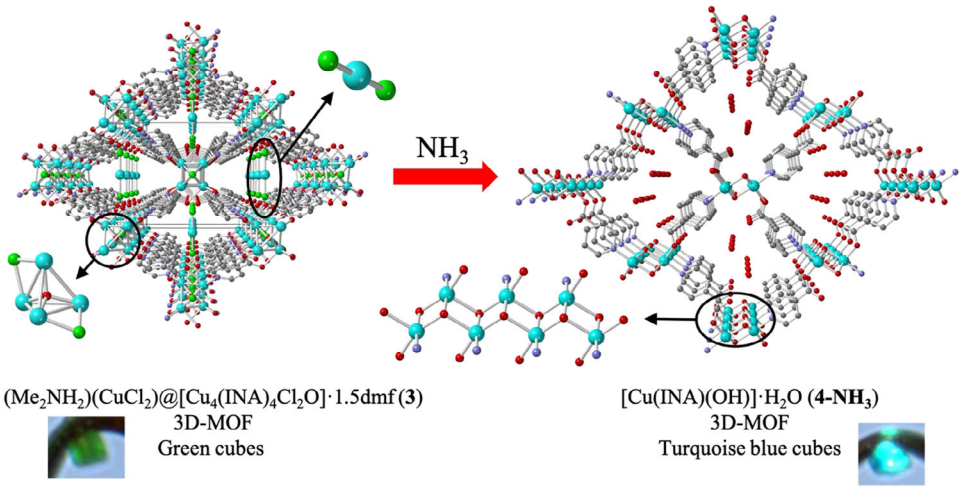

Figure 6. SC-SC transformation of the 3D MOF **3** into the 3D MOF **4-NH$_3$**. Color code: Cu = light blue, O = red, C = grey, Cl = green, and N = dark blue.

2.6.1. 3D-to-3D Conversion in NH_3 via SC-SC Transformation

When green single crystals of MOF **3** are exposed to vapors of concentrated aqueous NH_3, they undergo a rapid, naked-eye perceptible, color change from green to turquoise-blue single crystals of compound $[Cu(INA)(OH)]\cdot H_2O$ (**4-NH$_3$**) within a minute (Figure S3, Supporting Information). SCXRD analysis shows that **4-NH$_3$** is also a 3D MOF formed by $[Cu(\mu_3\text{-}OH)]_n$ chains connected with INA^- ligands (**Figure 6**).

SCXRD shows that **4-NH$_3$** crystallizes in the monoclinic $P2_1/n$ space group. The asymmetric unit is formed by one Cu^{II} ion, one deprotonated INA^- ligand and one OH^- anion (O1), both coordinated to the Cu^{II} atom, and one crystallization water molecule (OW1, Figure S41, Supporting Information). Therefore, the formula is $[Cu(INA)(OH)]\cdot H_2O$. The INA^- ligand bridges two Cu^{II} centers through its pyridine N-atom (N1) and one carboxylate O atom (O6B, Figure S42, Supporting Information), whereas the bridging OH^- ligand acts as a μ_3-OH^- bridge connecting three Cu^{II} centers (Figure S43, Supporting Information). Bond valence sum calculations show a value of 1.485 for O1, suggesting, along with the charge balance, the presence of these μ_3-OH^- bridges. The coordination geometry around the Cu^{II} ions is distorted square pyramidal ($\tau = 0.284$).[111] The basal positions are occupied by one N atom from one INA^- ligand, an O atom from a second INA^- ligand (O6B), and two O atoms of the μ_3-OH^- bridge. The axial position is occupied by an O atom from a third OH^- group (Figure S43, Supporting Information). As expected, the basal Cu-N (1.989(4) Å) and the Cu-O bond distances (in the range 1.939-2.006 Å) are much shorter than the axial one (2.256(3) Å, Table S4, Supporting Information).

The connectivity of the μ_3-OH^- bridge generates zigzag chains running along the *a* direction. The Cu-O bond distances within these chains are comparable to other $[Cu(\mu_3\text{-}OH)]_n$ based molecular clusters.[112,113] The Cu-hydroxide chains are connected by four INA^- ligands to four other Cu-hydroxide chains along the *bc* plane (Figure S44, Supporting Information), giving rise to a 3D structure with the formation of channels along the *a* direction, parallel to the $[Cu(\mu_3\text{-}OH)]_n^{n-}$ chains. These channels contain the crystallization water molecules (Figure 6). A search in the Cambridge Structural Database (CSD) shows that this is the first example of such metal-hydroxide coordination chains. We can, therefore, conclude that the post-synthetic treatment of MOF **3** with NH_3 results in a new structure based on an unprecedented metal-hydroxide chain. If we compare the structures of **3** and **4-NH$_3$**, we observe that the NH_3 molecules induce the rupture of the Cu-Cl bonds in the Cu_4OCl_2 tetrahedral cluster of **3**. This rupture facilitates the attack of the central oxido group by, most probably, a water molecule, generating two OH^- ligands that connect three Cu^{II} centers to form the $[Cu(OH)]_n^{n-}$ chain. The INA^- ligands change their coordination mode by breaking the long and weak Cu1-O11 bond (with a bond distance of 2.304(3) Å).

2.6.2. 3D-to-0D Conversion in HCl via DRST

Exposure of green single crystals of MOF **3** to vapors of concentrated aqueous HCl also results in a naked-eye perceptible color change from green to brown within a few minutes (Figure S4, Supporting Information). This brown compound is metastable and amorphous (Figure S45, Supporting Information). After a few minutes, it converts into a light-green liquid droplet, which subsequently forms lime-green crystals of **5-HCl** (Scheme S1, Supporting Information). The SCXRD analysis shows that **5-HCl** crystallizes in the triclinic *P*-1 space group. Its asymmetric unit contains one Cu^{II} ion, three coordinated chloride anions, one coordinated water molecule, and a protonated isonicotinic acid cation (Figure S46, Supporting Information). Application of the symmetry generates the formula $(H_2INA)_2[Cu_2Cl_6(H_2O)_2]$ (**5-HCl**). The structure of **5-HCl** consists of a centrosymmetric dichlorido-bridged copper dimer formulated as $[Cu_2Cl_6(H_2O)_2]^{2-}$ separated by protonated (at the N atom, Figure S46, Supporting Information) isonicotinic acid molecules (**Figure 7**). Each copper center has a distorted square pyramidal coordination geometry ($\tau = 0.257$).[111] The coordination sphere is formed by one axial and three basal chloride ligands and a basal water molecule. As expected, the Cu—Cl axial bond distance (2.856(6) Å) is much longer than the basal ones (in the range 2.2515–2.2852 Å), and

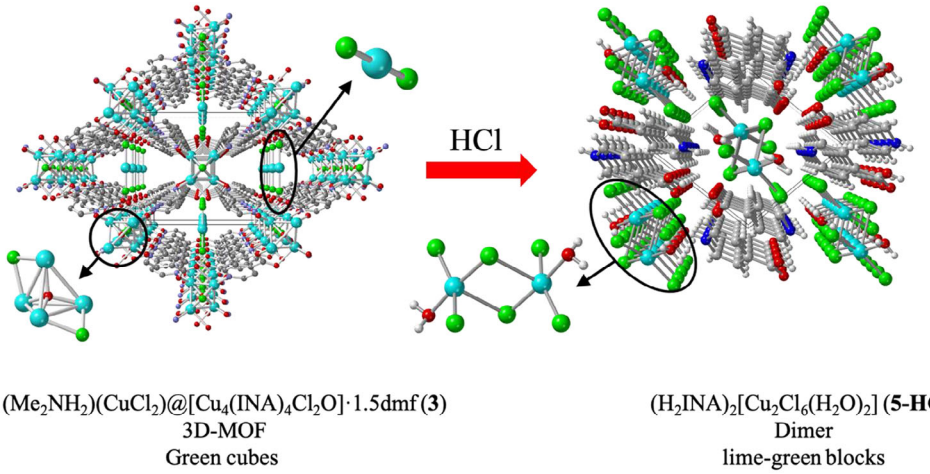

Figure 7. DRST of the 3D MOF **3** into the dimer **5-HCl**.

the Cu-O bond distance (1.9725(17) Å) is shorter than the Cu—Cl ones (Table S6, Supporting Information).

The overall negative charge of the $[Cu_2Cl_6(H_2O)_2]^{2-}$ anions is balanced by two protonated isonicotinic acid molecules. The transformation of **3** into **5-HCl** in the presence of HCl implies the rupture of the Cu_4OCl_2 into a dichlorido-bridged dimer through simultaneous replacement of the oxido group, accompanied by a double protonation of the isonicotinato ligands, which results in the breaking of the coordination bonds between these ligands and the Cu^{II} centers.

Besides the anion-cation interactions, the structure of **5-HCl** is further stabilized by a double H-bond formed between two protonated isonicotinic cations through their carboxylic groups and by a double Cl···H-N bond formed between the H atom linked to the pyridine N atom (H1) and the $[Cu_2Cl_6(H_2O)_2]^{2-}$ anions, giving rise to H-bonded layers parallel to the *ab* plane (Figure S47 and Table S13, Supporting Information). These H-bonded layers are further connected by an O-H···Cl interaction perpendicular to the layers (Figure S48, Supporting Information).

Interestingly, compound **3** also exhibits similar DRST-type behavior in the presence of HBr, HI, and HNO_3; however, we have not been able to obtain high-quality single crystals to determine the crystal structures of the resulting compounds. On the other hand, **3** is stable for more than a week in the presence of H_2SO_4 and H_3PO_4 vapors. Such selectivity can be attributed to either the lower vapor pressure of H_2SO_4 and H_3PO_4 or size and charge selectivity.

2.6.3. 3D-to-3D Conversion in HCOOH with Selective Uptake of $Me_2NH_2^+$ Cations via DRST

MOF **3** undergoes a structural transformation via DRST in the presence of formic acid vapor. It shows a drastic color change from green to sea-green upon exposure to formic acid vapor (Figure S5, Supporting Information), and converts into a liquid drop, which generates very small sea-green single crystals of compound $(Me_2NH_2)[Cu(HCOO)_3]$ (**6-For**, **Figure 8**). X-ray structural analysis shows that **6-For** crystallizes in the monoclinic *I2/a* space group. The asymmetric unit contains one Cu^{II} center, located on a special position, one and a half formate anions, and half $Me_2NH_2^+$ cation (Figure S49, Supporting Information). Application of the symmetry generates the formula

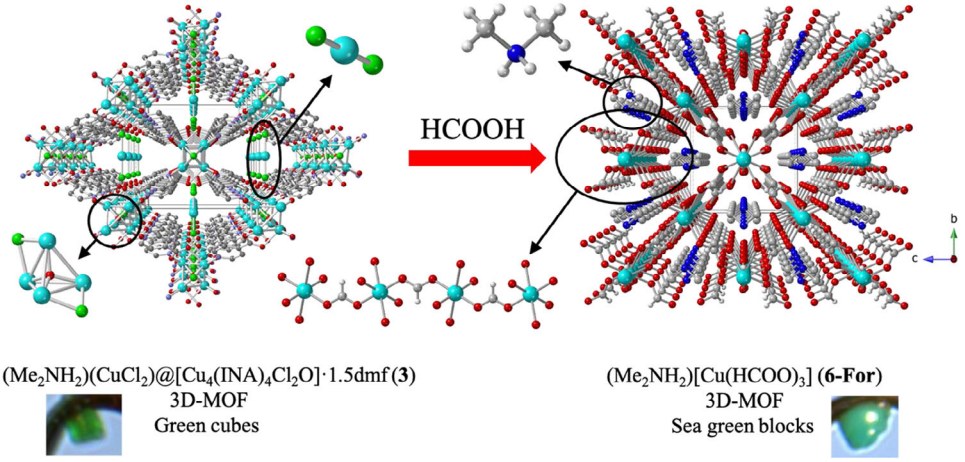

Figure 8. DRST of the 3D MOF **3** into the 3D MOF **6-For**.

Table 1. Balanced reactions and energy are required for the structural transformation of MOFs **2** and **3**.

Reaction	E [kJ mol^{-1}]
2 [2] + 4 $CuCl_2$ + H_2O → [3] + CO_2 + 2 HCl + $HCuCl_2$	−9686
[3] + 2 NH_3 + 7 H_2O → 4 **[4-NH$_3$]** + $Me_2NH_2(CuCl_2)$ + ½ dmf + 2 NH_4Cl	−636
[3] + 10 HCl + 3 H_2O → 2 **[5-HCl]** + $Me_2NH_2(CuCl_2)$ + ½ dmf	−883
[3] + 3 HCOOH → **[6-For]** + $HCuCl_2$ + $CuCl_2$ + $[Cu_2(INA)_4]$ + H_2O + ½ dmf	−31.8
[3] + 8 HAc + 3 H_2O → 2 **[7-Ac]** + $Me_2NH_2(CuCl_2)$ + 2 HCl + 4 HINA + ½ dmf	−862

[2] = $[Cu(INA)_2]$·dmf; [3] = $(Me_2NH_2)(Cu^ICl_2)@[Cu_4(INA)_4Cl_2O]$·1.5dmf; **[4-NH$_3$]** = $[Cu(INA)(OH)]·H_2O$; **[5-HCl]** = $(HINA)_2[Cu_2Cl_6(H_2O)_2]$; **[6-For]** = $(Me_2NH_2)[Cu(HCOO)_3]$; **[7-Ac]** = $[Cu_2(CH_3COO)_4]·2H_2O$; INA^- = $C_6H_4NO_2$, dmf = C_3H_7NO, HAc = CH_3COOH.

$(Me_2NH_2)[Cu(HCOO)_3]$. The structure of **6-For** consists of a 3D array formed by three orthogonal anionic $[Cu(HCOO)_3]_n^{n-}$ chains running along the *a* direction and along the (011) and (01-1) directions. Each chain is, therefore, connected to four other chains to generate a 3D structure with square channels where the charge-balancing $Me_2NH_2^+$ cations are located (Figure 8). Each Cu^{II} ion is, therefore, connected to six other Cu^{II} centers through six formato ligands (Figure S50, Supporting Information). The anionic $[Cu(HCOO)_3]_n^{n-}$ chains are formed by CuO_6 octahedra with a large Jahn-Teller elongation (the Cu-O axial bond distance is 2.452(5) Å, whereas the equatorial ones are 1.967(4) and 1.970(4) Å, Table S8, Supporting Information). The equatorial planes of consecutive Cu^{II} centers in the chains are almost orthogonal (Figure S51, Supporting Information).

Besides the anion-cation interactions, the structure of **6-For** is further stabilized by the formation of a strong H-bond between one of the H atoms (H10A) linked to the N atom of the $Me_2NH_2^+$ cations and the O3 atom from the formate anion, with the following structural parameters: N-H = 0.910 Å, H···O = 1.907 Å, N···O = 2.806 Å and <N-H···O> = 169.3° (Figure S52, Supporting Information).

It is noteworthy to mention that during the structural transformation via DRST, the newly obtained single crystals of **6-For** selectively incorporate the charge-balancing $Me_2NH_2^+$ cations from the solution (instead of other possible cations), further confirming the presence of these $Me_2NH_2^+$ cations in the pristine MOF **3**. Another interesting fact is the formation of an anionic $[Cu(HCOO)]_n^{n-}$ chain, in contrast to the neutral copper(II) formate[114] and basic copper(II) formate structures[115,116] formed when Cu^{II} is reacted with formic acid or formate anions, respectively. This fact suggests that the presence of the $Me_2NH_2^+$ cations may facilitate or induce the formation of the anionic $[Cu(HCOO)]_n^{n-}$ chains.

Finally, as mentioned before, MOF **3** undergoes an additional DRST in the presence of acetic acid vapors to produce the well-known dimeric copper(II) acetate complex $[Cu_2(CH_3COO)_4(H_2O)_2]$ (Figure S53, Supporting Information).[59]

2.7. Magnetic Properties of Compounds 5-HCl and 6-For

Compound **5-HCl** shows moderate antiferromagnetic Cu···Cu interactions through the double Cl bridge (Figure S54, Supporting Information), as expected for a double chloride bridged Cu^{2+} dimer when the Cl^- bridges connect axial with basal positions.[117] Compound **6-For** shows a moderate antiferromagnetic Cu···Cu exchange, as expected for Cu^{II} ions connected through single *anti-anti* carboxylate bridges (Figure S55, Supporting Information).[118] A more detailed description of the magnetic properties can be found in the Supporting Information.

2.8. Theoretical Analysis on the Selective Gas-Solid Reaction of MOF 3

To gain insight into this versatile and selective gas-solid reaction of MOF-**3**, we have performed a theoretical DFT study of the structural transformations through gas-solid reactions using the FHI-aims code[109,119] with the PBE exchange-correlation functional[120] and including dispersion effects via a many-body approach[121] for the structural optimization of the unit cells. The energy calculation for the optimized structures was performed using the hybrid B3LYP functional.[122] All the calculations were carried out using a tight quality basis set and (1,1,8,4,8,2) *k*-points for **2**, **3**, **4-NH$_3$**, **6-For**, **5-HCl**, and **7-Ac**, respectively. To calculate the product molecules of the chemical processes, solvent effects were included with the Multipole Expansion (MPE) implicit solvation method[123,124] using the single cavity approach implemented in the FHI-aims code. In calculating the reaction energies involved in the SC-SC transformations from compound **3**, we have considered that the reactive molecule is in the gas phase, as experimentally, the reactions are done by exposing the crystal to the vapors of the acids/base. **Table 1** shows the balanced calculated reactions and their reaction energies. For the periodic systems in Table 1, we have considered the formula unit.

The DFT-optimized unit cells from experimental SCXRD data are provided in Table S14 in the Supporting Information. The comparison with the experimental X-ray diffraction data shows that the optimized unit cell volumes for the six compounds are slightly larger than the experimental ones, the smallest (1.2%) and the largest (4.1%) difference values being found for **7-Ac** and **4-NH$_3$**, respectively. These relatively small error values confirm the excellent accuracy of the DFT method in predicting these periodic structures.

3. Conclusion

In summary, we present a systematic study of the gas-solid reaction of a copper MOF encapsulating an ion-pair, along with its NIR activity. This MOF, formulated as $(Me_2NH_2)(Cu^ICl_2)@[Cu_4(INA)_4Cl_2O]$·1.5dmf (**3**) has been synthesized by a two-step method and contains both $Me_2NH_2^+$

cations and $CuCl_2^-$ anions within the void space. MOF **3** shows multiple and selective structural transformations upon exposure to a diverse range of chemically reactive and volatile gas species. Thus: (i) MOF **3** undergoes ultrafast SC-SC structural transformation in the presence of NH_3 vapor to form the 3D MOF $[Cu(INA)(OH)]\cdot H_2O$ (**4-NH$_3$**) containing an unprecedented $[Cu(\mu_3\text{-}OH)]_n$ chain; (ii) MOF **3** is stable under Et_3N vapor over seven days; (iii) MOF **3** undergoes a dissolution recrystallisation-mediated structural transformation in the presence of HCl vapor to form $(HINA)_2[Cu_2Cl_6(H_2O)_2]$ (**5-HCl**), containing dichlorido-bridged copper dimers; (iv) MOF **3** shows DRST upon exposure to formic acid vapor to form a 3D anionic copper(II) formate framework with selective encapsulation of $Me_2NH_2^+$ cations from the parent MOF; (v) MOF **3** forms the well-known copper(II) acetate paddle-wheel structure in the presence of acetic acid via DRST, and (vi) MOF **3** shows structural stability over a wide range of volatile chemical vapors like H_2SO_4, H_3PO_4, triethylamine, acetone, methanol, ethanol and acetonitrile. All these structural transformations have been optimized with DFT calculations, with excellent agreement between the experimental X-ray and the optimized structures. As far as we know, this is the first example of multiple and selective gas-solid reaction of a single MOF to yield two new MOFs and one new compound. Moreover, the encapsulation of $CuCl_2^-$ in MOF **3** leads to an unusual UV-NIR-MIR absorption and NIR emission, also unprecedented in transition metal-based MOFs. Theoretical calculations suggest that the reduction of Cu^{II} to Cu^{I} in the framework host is the primary reason for such an unusual optical phenomenon. This study shows a new way to develop NIR-active materials through encapsulation of metal halides within the void space of MOFs.

Supporting Information

Supporting Information is available from the Wiley Online Library or from the author.

Acknowledgements

This study forms part of the Advanced Materials program and was supported by the Spanish MCIN with funding from European Union NextGeneration EU (PRTR- C17.I1) and the Generalitat Valenciana (projects MFA-2022-057, MFA-2022-017, and MFA-2022-031). We also thank the Grants PID2021-125907NB-I00, PID2021-122464NB-I00, PID2021-128569NB-I00, and María de Maeztu CEX2021-001202-M, funded by MCIN/AEI/10.13039/501100011033 and by "ERDF A way of making Europe" and projects CIPROM-2022-060 and CIPROM/2022/57 from the Generalitat Valenciana, for financial support. E.R. thanks the Generalitat de Catalunya for the 2021-SGR-00286 grant, and for an ICREA Academia and CSUC and BSC centers for computational resources. A.F.-R. acknowledges the Generalitat Valenciana for the CIAPOS/2023/316 grant. We also thank the Generalitat Valenciana (IDIFEDER/2021/075) for financing the acquisition of the single crystal X-ray diffractometer.

Conflict of Interest

The authors declare no conflict of interest.

Data Availability Statement

The data that support the findings of this study are available from the corresponding author upon reasonable request.

Keywords

dissolution recrystallization structural transformation in MOFs, gas-solid reactivity in MOFs, ion-pair guests in MOFs, near-IR activity in MOFs, single-crystal-to-single-crystal structural transformation in MOFs

Received: July 14, 2025
Revised: September 16, 2025
Published online:

[1] G. K. Kole, J. J. Vittal, *Chem. Soc. Rev.* **2013**, *42*, 1755.
[2] V. V. Boldyrev *Reactivity of Solids: Past, Present and Future*, Blackwell Science Oxford, UK **1996**.
[3] F. Toda *Organic Solid State Reactions*, Springer Science & Business Media, Berlin **2005**.
[4] G. Schmidt, *Pure Appl. Chem.* **1971**, *27*, 647.
[5] D. Braga, F. Grepioni, *Angew. Chem., Int. Ed.* **2004**, *43*, 4002.
[6] P. Naumov, D. P. Karothu, E. Ahmed, L. Catalano, P. Commins, J. Mahmoud Halabi, M. B. Al-Handawi, L. Li, *J. Am. Chem. Soc.* **2020**, *142*, 13256.
[7] J. Liu, J. Du, Y. Wu, Y. Zhao, X. Zhou, D. Li, *Chem. Commun.* **2017**, *53*, 12950.
[8] H. Li, M. Eddaoudi, M. O'Keeffe, O. M. Yaghi, *Nature* **1999**, *402*, 276.
[9] I. Senkovska, V. Bon, A. Mosberger, Y. Wang, S. Kaskel, *Adv. Mater.* **2025**, 2414724.
[10] S. T. Meek, J. A. Greathouse, M. D. Allendorf, *Adv. Mater.* **2011**, *23*, 249.
[11] T. Luo, L. Gilmanova, S. Kaskel, *Coord. Chem. Rev.* **2023**, *490*, 215210.
[12] I. E. Khalil, J. Fonseca, M. R. Reithofer, T. Eder, J. M. Chin, *Coord. Chem. Rev.* **2023**, *481*, 215043.
[13] T. De Villenoisy, X. Zheng, V. Wong, S. S. Mofarah, H. Arandiyan, Y. Yamauchi, P. Koshy, C. C. Sorrell, *Adv. Mater.* **2023**, *35*, 2210166.
[14] K. Sumida, D. L. Rogow, J. A. Mason, T. M. McDonald, E. D. Bloch, Z. R. Herm, T. Bae, J. R. Long, *Chem. Rev.* **2012**, *112*, 724.
[15] G. C. Thaggard, B. K. M. Kankanamalage, K. C. Park, J. Lim, M. A. Quetel, M. Naik, N. B. Shustova, *Adv. Mater.* **2024**, 2410067.
[16] H. Zhou, J. R. Long, O. M. Yaghi, *Chem. Rev.* **2012**, *112*, 673.
[17] R. Saha, C. J. Gómez-García, *Chem. Soc. Rev.* **2024**, *53*, 9490.
[18] Y. Jo, Y. K. Jo, J. Lee, H. W. Jang, I. Hwang, D. J. Yoo, *Adv. Mater.* **2023**, *35*, 2206842.
[19] R. Saha, K. Gupta, C. J. Gómez García, *Cryst. Growth Des.* **2024**, *24*, 2235.
[20] Y. Ye, L. Gong, S. Xiang, Z. Zhang, B. Chen, *Adv. Mater.* **2020**, *32*, 1907090.
[21] J. Hao, X. Xu, H. Fei, L. Li, B. Yan, *Adv. Mater.* **2018**, *30*, 1705634.
[22] E. Miguel-Casañ, G. R. Orton, D. E. Schier, N. R. Champness, *Adv. Mater.* **2025**, 2414509.
[23] Z. Chang, *Coord. Chem. Rev.* **2023**, *476*, 214921.
[24] Y. Jiao, Y. Zuo, H. Yang, X. Gao, C. Duan, *Coord. Chem. Rev.* **2021**, *430*, 213648.
[25] M. D. Allendorf, M. E. Foster, F. Léonard, V. Stavila, P. L. Feng, F. P. Doty, K. Leong, E. Y. Ma, S. R. Johnston, A. A. Talin, *J. Phys. Chem. Lett.* **2015**, *6*, 1182.
[26] K. Kim, J. T. Culp, D. C. Sorescu, J. E. Ellis, P. C. Cvetic, B. H. Howard, P. R. Ohodnicki, A. L. Goodman, J. A. Steckel, H. T. Kwon, *Growth Des* **2021**, *21*, 817.
[27] K. Biradha, A. Goswami, R. Moi, S. Saha, *Dalton Trans.* **2021**, *50*, 10655.
[28] R. E. Morris, L. Brammer, *Chem. Soc. Rev.* **2017**, *46*, 5444.

[29] J. J. Vittal, H. S. Quah, *Coord. Chem. Rev.* **2017**, *342*, 1.
[30] F. Bigdeli, C. T. Lollar, A. Morsali, H. Zhou, *Angew. Chem., Int. Ed.* **2020**, *59*, 4652.
[31] Y. Xiang, S. Wei, T. Wang, H. Li, Y. Luo, B. Shao, N. Wu, Y. Su, L. Jiang, J. Huang, *Coord. Chem. Rev.* **2025**, *523*, 216263.
[32] J. Pang, M. Wu, J. Qin, C. Liu, C. T. Lollar, D. Yuan, M. Hong, H. Zhou, *Chem. Mater.* **2019**, *31*, 8787.
[33] C. Castillo-Blas, A. M. Chester, D. A. Keen, T. D. Bennett, *Chem. Soc. Rev.* **2024**, 3606.
[34] C. L. Jones, A. J. Tansell, T. L. Easun, *J. Mater. Chem. A* **2016**, *4*, 6714.
[35] P. Vervoorts, J. Stebani, A. S. Mendez, G. Kieslich, *ACS Materials Lett.* **2021**, *3*, 1635.
[36] S. Zhao, C. Tan, C. He, P. An, F. Xie, S. Jiang, Y. Zhu, K. Wu, B. Zhang, H. Li, *Nat. Energy* **2020**, *5*, 881.
[37] G. Mínguez Espallargas, L. Brammer, J. van de Streek, K. Shankland, A. J. Florence, H. Adams, *J. Am. Chem. Soc.* **2006**, *128*, 9584.
[38] P. Smart, C. A. Mason, J. R. Loader, A. J. Meijer, A. J. Florence, K. Shankland, A. J. Fletcher, S. P. Thompson, M. Brunelli, A. H. Hill, *Chem. - Eur. J.* **2013**, *19*.
[39] K. C. Stylianou, J. Rabone, S. Y. Chong, R. Heck, J. Armstrong, P. V. Wiper, K. E. Jelfs, S. Zlatogorsky, J. Bacsa, A. G. McLennan, *J. Am. Chem. Soc.* **2012**, *134*, 20466.
[40] R. Saha, S. K. Dey, S. Biswas, A. D. Jana, S. Kumar, *Cryst. Growth Des.* **2013**, *13*, 2135.
[41] J. Lu, T. Paliwala, S. C. Lim, C. Yu, T. Niu, A. J. Jacobson, *Inorg. Chem.* **1997**, *36*, 923.
[42] G. González Miera, A. Bermejo Gómez, P. J. Chupas, B. Martín-Matute, K. W. Chapman, A. E. Platero-Prats, *Inorg. Chem.* **2017**, *56*, 4576.
[43] M. Gupta, J. J. Vittal, *Coord. Chem. Rev.* **2021**, *435*, 213789.
[44] S. S. Kaye, A. Dailly, O. M. Yaghi, J. R. Long, *J. Am. Chem. Soc.* **2007**, *129*, 14176.
[45] C. Serre, F. Millange, C. Thouvenot, M. Noguès, G. Marsolier, D. Louër, G. Férey, *J. Am. Chem. Soc.* **2002**, *124*, 13519.
[46] I. J. Vitórica-Yrezábal, S. Libri, J. R. Loader, G. Minguez Espallargas, M. Hippler, A. J. Fletcher, S. P. Thompson, J. E. Warren, D. Musumeci, M. D. Ward, L. Brammer, *Chem. - Eur. J.* **2015**, *21*, 8799.
[47] G. Minguez Espallargas, J. van de Streek, P. Fernandes, A. J. Florence, M. Brunelli, K. Shankland, L. Brammer, *Angew. Chem., Int. Ed.* **2010**, *49*, 8892.
[48] E. Coronado, M. Gimenez-Marques, G. M. Espallargas, L. Brammer, *Nature Commun* **2012**, *3*, 828.
[49] C. J. Adams, M. F. Haddow, M. Lusi, A. G. Orpen, *Proc. Natl. Acad. Sci. USA* **2010**, *107*, 16033.
[50] M. J. Katz, T. Ramnial, H. Yu, D. B. Leznoff, *J. Am. Chem. Soc.* **2008**, *130*, 10662.
[51] X. Cui, A. N. Khlobystov, X. Chen, D. H. Marsh, A. J. Blake, W. Lewis, N. R. Champness, C. J. Roberts, M. Schröder, *Chem. - Eur. J.* **2009**, *15*, 8861.
[52] S. Lee, J. L. Mancuso, K. N. Le, C. D. Malliakas, Y. Bae, C. H. Hendon, T. Islamoglu, O. K. Farha, *ACS Materials Lett* **2020**, *2*, 499.
[53] M. Tu, S. Wannapaiboon, R. A. Fischer, *J. Mater. Chem. A* **2020**, *8*, 13710.
[54] L. A. Brandner, M. Linares-Moreau, G. Zhou, H. Amenitsch, S. Dal Zilio, Z. Huang, C. Doonan, P. Falcaro, *Chem. Sci.* **2023**, *14*, 12056.
[55] C. L. Johnson, D. J. Storm, M. A. Sajjad, M. R. Gyton, S. B. Duckett, S. A. Macgregor, A. S. Weller, M. Navarro, J. A. Campos, *Angew. Chem., Int. Ed.* **2024**, *63*, 202404264.
[56] J. Sundberg, L. J. Cameron, P. D. Southon, C. J. Kepert, C. J. McKenzie, *Chem. Sci.* **2014**, *5*, 4017.
[57] O. V. Zenkina, E. C. Keske, R. Wang, C. M. Crudden, *Angew. Chem., Int. Ed.* **2011**, *50*, 8100.
[58] Z. Huang, P. S. White, M. Brookhart, *Nature* **2010**, *465*, 598.
[59] J. N. Van Niekerk, F. Schoening, *Acta Cryst* **1953**, *6*, 227.
[60] T. N. Nguyen, F. M. Ebrahim, K. C. Stylianou, *Coord. Chem. Rev.* **2018**, *377*, 259.
[61] A. Foucault-Collet, K. A. Gogick, K. A. White, S. Villette, A. Pallier, G. Collet, C. Kieda, T. Li, S. J. Geib, N. L. Rosi, *Proc. Natl. Acad. Sci. USA* **2013**, *110*, 17199.
[62] T. N. Nguyen, S. V. Eliseeva, A. Gładysiak, S. Petoud, K. C. Stylianou, *J. Mater Chem. A* **2020**, *8*, 10188.
[63] C. Liu, S. V. Eliseeva, T. Luo, P. F. Muldoon, S. Petoud, N. L. Rosi, *Chem. Sci.* **2018**, *9*, 8099.
[64] B. Guo, J. Yin, N. Li, Z. Fu, X. Han, J. Xu, X. Bu, *Adv. Optical Mater.* **2021**, *9*, 2100283.
[65] Z. M. Soilis, T. H. Choi, J. Brennan, R. R. Frontiera, J. K. Johnson, N. L. Rosi, *Chem. Mater.* **2023**, *35*, 7741.
[66] P. F. Muldoon, G. Collet, S. V. Eliseeva, T. Luo, S. Petoud, N. L. Rosi, *J. Am. Chem. Soc.* **2020**, *142*, 8776.
[67] G. Collet, A. Hrvat, S. V. Eliseeva, C. Besnard, A. Kovalenko, S. Petoud, *Chem. Commun.* **2021**, *57*, 3351.
[68] T. Yan, Y. Li, J. Su, H. Wang, J. Zuo, *Chem. - Eur. J.* **2021**, *27*, 11050.
[69] K. Scanlan, A. L. Kanibolotsky, B. Breig, G. J. Hedley, P. J. Skabara, *J. Mater. Chem. C.* **2019**, *7*, 6582.
[70] F. Wang, J. Wu, Y. Zhang, S. Yang, N. Zhang, H. Li, T. Zhai, *Sci. China Mater.* **2022**, *65*, 451.
[71] P. Huang, Y. Zhang, P. Tsai, R. Chung, Y. Tsai, M. Leung, S. Lin, M. Fang, *Adv. Opt. Mater.* **2024**, *12*, 2302062.
[72] K. Waizump, M. Takuno, N. Fukushima, H. Masuda, *J. Coord. Chem.* **1998**, *44*, 269.
[73] C. Z. Lin, S. S. Chui, S. M. Lo, F. L. Shek, M. Wu, K. Suwinska, J. Lipkowski, I. D. Williams, *Chem. Commun.* **2002**, 1642.
[74] N. Okabe, T. Nakamura, H. Fukuda, *Acta Cryst. C* **1993**, *49*, 1761.
[75] M. Cao, J. Wu, J. Liang, B. Ye, *Cryst. Growth Des.* **2010**, *10*, 4934.
[76] M. Almáši, Z. Vargová, R. Gyepes, R. Varga, V. Zeleňák, *Inorg. Chem. Commun.* **2014**, *46*, 118.
[77] L. Wang, T. Zeng, G. Liao, Q. Cheng, Z. Pan, *Polyhedron* **2019**, *157*, 152.
[78] Y. Liu, A. Yang, X. Zhang, Z. Sun, W. Li, Y. Wang, J. Luan, H. Liu, *J. Env. Chem. Eng.* **2022**, *10*, 108215.
[79] B. K. Das, S. J. Bora, M. Chakrabortty, L. Kalita, R. Chakrabarty, R. Barman, *J. Chem. Sci.* **2006**, *118*, 487.
[80] R. Saha, A. Sharma, A. I. Siddiqui, S. Benmansour, J. Ortega-Castro, A. Frontera, B. Mondal, M. S. Lah, C. J. G. García, *Chem. Sci.* **2025**, *16*, 9501.
[81] T. Lian, S. Chen, *Inorg. Chem. Commun.* **2012**, *18*, 8.
[82] J. Jiang, Z. Lu, M. Zhang, J. Duan, W. Zhang, Y. Pan, J. Bai, *J. Am. Chem. Soc.* **2018**, *140*, 17825.
[83] S. A. Sahadevan, N. Monni, A. Abherve, G. Cosquer, M. Oggianu, G. Ennas, M. Yamashita, N. Avarvari, M. L. Mercuri, *Inorg. Chem.* **2019**, *58*, 13988.
[84] I. Jeon, B. Negru, R. P. V. Duyne, T. D. Harris, *J. Am. Chem. Soc.* **2015**, *137*, 15699.
[85] K. A. Collins, R. J. Saballos, M. S. Fataftah, D. Puggioni, J. M. Rondinelli, D. E. Freedman, *Chem. Sci.* **2020**, *11*, 5922.
[86] N. Ichiishi, A. J. Canty, B. F. Yates, M. S. Sanford, *Organometallics* **2014**, *33*, 5525.
[87] J. N. Muzart, *Tetrahedron* **2009**, *65*, 8313.
[88] A. Y. Malkhasian, M. E. Finch, B. Nikolovski, A. Menon, B. E. Kucera, *Inorg. Chem.* **2007**, *46*, 2950.
[89] J. J. Teo, Y. Chang, H. C. Zeng, *Langmuir* **2006**, *22*, 7369.
[90] D. Guk, A. Naumov, O. Krasnovskaya, V. Tafeenko, A. Moiseeeva, V. Pergushov, M. Melnikov, N. Zyk, A. Majouga, E. Belolglazkina, *Dalton Trans.* **2020**, *49*, 14528.
[91] A. Kitabayashi, Y. Ono, T. Taketsugu, M. Sawamura, K. Higashida, *Chem. - Eur. J.* **2023**, *29*, 202301673.
[92] H. Herrmann, E. Kaifer, H. Himmel, *Chem. - Eur. J.* **2017**, *23*, 5520.

[93] T. S. Sukhikh, R. M. Khisamov, D. A. Bashirov, V. Y. Komarov, M. S. Molokeev, A. A. Ryadun, E. Benassi, S. N. Konchenko, *Cryst. Growth Des.* **2020**, *20*, 5796.
[94] F. Nahra, K. Van Hecke, A. R. Kennedy, D. J. Nelson, *Dalton Trans.* **2018**, *47*, 10671.
[95] B. J. Charette, P. J. Griffin, C. M. Zimmerman, L. Olshansky, *Dalton Trans.* **2022**, *51*, 6212.
[96] M. Feliz, E. Guillamón, R. Llusar, C. Vicent, S. Stiriba, J. Pérez-Prieto, M. Barberis, *Chem. - Eur. J.* **2006**, *12*, 1486.
[97] F. A. Cotton, C. A. Murillo, L. E. Roy, H. Zhou, *Inorg. Chem.* **2000**, *39*, 1743.
[98] B. Bouhafs, H. Heireche, W. Sekkal, H. Aourag, M. Certier, *Phys. Lett. A* **1998**, *240*, 257.
[99] D. Banerjee, B. Saparov, *Chem. Mater.* **2023**, *35*, 3364.
[100] S. K. Sachan, G. Anantharaman, *Inorg. Chem.* **2022**, *61*, 18340.
[101] W. Wang, D. Zeng, J. Wang, B. Cui, T. Jia, R. Li, H. Chu, Y. Zhang, L. Zhang, W. Wang, *Green Chem.* **2023**, *25*, 8863.
[102] X. Liang, R. K. Gupta, Y. Li, H. Ma, L. Gao, C. Tung, D. Sun, *Inorg. Chem.* **2020**, *59*, 2680.
[103] Y. Gao, L. Zhang, Y. Gu, W. Zhang, Y. Pan, W. Fang, J. Ma, Y. Lan, J. Bai, *Chem. Sci.* **2020**, *11*, 10143.
[104] C. Chan, K. Cheung, W. H. Lam, E. C. Cheng, N. Zhu, S. W. Choi, V. W. Yam, *Chem. As. J.* **2006**, *1*, 273.
[105] L. L. Zhang, G. Zhou, G. Zhou, H. Lee, N. Zhao, O. V. Prezhdo, T. C. Mak, *Chem. Sci.* **2019**, *10*, 10122.
[106] L. Wang, Z. Xiong, J. Zhi Sun, F. Huang, H. Zhang, B. Zhong Tang, *Angew. Chem.* **2024**, *136*, 202318245.
[107] S. Agrawal, D. Shil, A. Gupta, S. Mukherjee, *Nanoscale* **2024**, *16*, 20556.
[108] W. Liao, J. Zhang, S. Yin, H. Lin, X. Zhang, J. Wang, H. Wang, K. Wu, Z. Wang, Y. Fan, *Nature Commun* **2018**, *9*, 2401.
[109] V. Blum, R. Gehrke, F. Hanke, P. Havu, V. Havu, X. Ren, K. Reuter, M. Scheffler, *Comput. Phys. Commun.* **2009**, *180*, 2175.
[110] A. V. Krukau, O. A. Vydrov, A. F. Izmaylov, G. E. Scuseria, *J. Chem. Phys.* **2006**, 125.
[111] A. W. Addison, T. N. Rao, J. Reedijk, J. van Rijn, G. C. Verschoor, *J. Chem. Soc., Dalton Trans.* **1984**, 1349.
[112] X. Li, D. Cheng, J. Lin, Z. Li, Y. Zheng, *Cryst. Growth Des.* **2008**, *8*, 2853.
[113] Y. Zheng, D. Cheng, B. Liu, W. Huang, *Dalton Trans.* **2011**, *40*, 277.
[114] V. N. Krasil'nikov, V. P. Zhukov, E. V. Chulkov, I. V. Baklanova, D. G. Kellerman, O. I. Gyrdasova, T. V. Dyachkova, A. P. Tyutyunnik, *J. Alloys Compounds* **2020**, *845*, 156208.
[115] H. Euler, B. Barbier, A. Kirfe, S. Haselof, G. Eggert, *New Cryst. Struct.* **2009**, *224*, 643.
[116] H. Tamura, K. Ogawa, W. Mori, M. Kishita, *Inorg. Chim. Acta* **1981**, *54*, L87.
[117] A. Rodríguez-Fortea, P. Alemany, S. Alvarez, E. Ruiz, *Inorg. Chem.* **2002**, *41*, 3769.
[118] A. Rodríguez-Fortea, P. Alemany, S. Alvarez, E. Ruiz, *Chem. -Eur. J.* **2001**, *7*, 627.
[119] S. V. Levchenko, X. Ren, J. Wieferink, R. Johanni, P. Rinke, V. Blum, M. Scheffler, *Comput. Phys. Commun.* **2015**, *192*, 60.
[120] J. P. Perdew, K. Burke, M. Ernzerhof, *Phys. Rev. Lett.* **1996**, *77*, 3865.
[121] A. Tkatchenko, R. A. DiStasio, R. Car, M. Scheffler, *Phys. Rev. Lett.* **2012**, *108*, 236402.
[122] A. D. Becke, *J. Chem. Phys.* **1993**, *98*, 5648.
[123] J. Filser, K. Reuter, H. Oberhofer, *J. Chem. Theory Comput.* **2022**, *18*, 461.
[124] M. Sinstein, C. Scheurer, S. Matera, V. Blum, K. Reuter, H. Oberhofer, *J. Chem. Theory Comput.* **2017**, *13*, 5582.